HOKKAIDO UNIVERSITY

| | |
|---|---|
| Title | Amorphous-to-crystalline transition of silicon-incorporated anodic ZrO2 and improved dielectric properties |
| Author(s) | Koyama, S.; Aoki, Y.; Nagata, S. et al. |
| Citation | Electrochimica Acta, 55(9), 3144-3151<br>https://doi.org/10.1016/j.electacta.2010.01.063 |
| Issue Date | 2010-03-30 |
| Doc URL | https://hdl.handle.net/2115/43907 |
| Type | journal article |
| File Information | amorphous.pdf |

Hokkaido University Collection of Scholarly and Academic Papers : HUSCAP

# Amorphous-to-crystalline transition of silicon incorporated anodic $ZrO_2$ and improved dielectric properties

S. Koyama [a], Y. Aoki [a], S. Nagata [b], H. Kimura [b], H. Habazaki [a,*]

[a] Graduate School of Engineering, Hokkaido University, N13-W8, Kita-ku, Sapporo 060-8628, Japan

[b] Institute for Materials Research, Tohoku University, 2-1-1, Katahira, Sendai 980-8577, Japan

*Corresponding author. Tel./fax: +81 11 706 6575.

*E-mail address:* habazaki@eng.hokudai.ac.jp (H. Habazaki).

**Abstract**

Sputter-deposited zirconium and Zr–16 at.% Si alloy have been anodized to various voltages at several formation voltages in 0.1 mol $dm^{-3}$ ammonium pentaborate electrolyte at 298 K for 900 s. The resultant anodic films have been characterized using X-ray diffraction, transmission electron microscopy, Rutherford backscattering spectroscopy, glow discharge optical emission spectroscopy, and electrochemical impedance spectroscopy. The anodic oxide films formed on Zr–16 at.% Si are amorphous up to 30 V, but the outer part of the anodic oxide films crystallizes at higher formation voltages. This is in contrast to the case of sputter-deposited zirconium, on which the crystalline anodic oxide films, composed mainly of monoclinic $ZrO_2$, are developed even at low formation voltages. The outer crystalline layer on the Zr-16 at.% Si consists of a high-temperature stable tetragonal phase of $ZrO_2$. Due to immobile nature of silicon species, silicon-free outermost layer is formed by simultaneous migrations of $Zr^{4+}$ ions outwards and $O^{2-}$ ions inwards. An intermediate crystalline oxide layer, in which silicon content is lower in comparison with that in the innermost layer, is developed at the boundary of the crystalline layer and amorphous layer. Capacitances of the anodic zirconium oxide are highly enhanced by incorporation of silicon due to reduced film thickness, even though the permittivity of anodic oxide decreases with silicon incorporation.

*Keywords:* Anodic oxide; $ZrO_2$–$SiO_2$; Amorphous-to-crystalline transition; Ionic transport; Dielectric properties

## 1. Introduction

$ZrO_2$ is an important inorganic material due to many useful properties, including its high strength and stability at high temperatures, oxide ion conductivity at elevated temperatures and radiation-resistant properties. These features make $ZrO_2$ attractive for high-temperature applications, oxide ion sensors, solid electrolyte for fuel cells and as a material in nuclear industry [1-3]. Moreover, in recent years, $ZrO_2$ has been proposed as a promising dielectric material in metal-oxide semiconductor devices [4, 5].

Thin films of $ZrO_2$, necessary for capacitor applications, can be prepared by a range of methods, using physical vapor deposition [6], chemical vapor deposition [7], atomic layer deposition [4], chemical solution deposition [8, 9] and anodizing [10, 11]. Anodizing has been extensively used to form dielectric oxide films on aluminum and tantalum for electrolytic capacitor applications. In last decade, it becomes also possible to form self-organized porous anodic oxide films on various valve metals by utilizing dilute fluoride-containing electrolytes [12-18]. Such films have attracted increasing attention due to potential widespread applications, including solar cells, catalysis, electrochromic windows, bio-implants and various nanodevices.

The formation of anodic oxide films on valve metals have been extensively studied, due to scientific interest of the ionic transport in growing anodic oxides under the high electric field, in addition to the practical importance of the anodic oxide films. Amorphous anodic oxide films are usually formed on many valve metals, including aluminium, bismuth, niobium, tantalum and tungsten. Anodizing of titanium results in the transition of an initially formed amorphous oxide to crystalline oxide at 5-10 V,

which causes oxygen gas generation within the anodic oxide film [19, 20]. Thus, the films with a high density of flaws are developed after crystallization The anodic films formed on zirconium and hafnium are generally crystalline, but the film growth proceeds at high current efficiency without gas generation [21]. The mechanism of film growth is also dependent upon whether anodic oxides are crystalline or amorphous. In growing amorphous anodic oxides, simultaneous migrations of cations outwards and anions inwards proceed in a cooperative manner, developing film material both at the film/electrolyte and metal/film interfaces, respectively [22]. On the other hand, crystalline anodic oxides, formed on zirconium and hafnium, grow predominantly at the metal/film interface by migration of anions inwards [23].

The crystalline structure of anodic oxide films formed on zirconium has been examined mainly by transmission electron microscopy. When magnetron sputtered zirconium is anodized in ammonium pentaborate electrolyte without pretreatment of the deposited surface, crystalline oxide films, consisting mainly of monoclinic $ZrO_2$, are developed [11]. The monoclinic phase of $ZrO_2$ is thermodynamically the most stable at ambient temperature. Amorphous and a high-temperature stable phase of cubic or tetragonal $ZrO_2$ are often found in the anodic oxide films formed on chemically polished zirconium, particularly at low formation voltages [24, 25]. The structure is also dependent upon the electrolyte [26, 27]. Such dependence should be associated with the incorporation of foreign species from electrolyte or pretreated bath.

Foreign species can be incorporated also from substrate by alloying of zirconium. Anodic film growth and film properties are examined for the Zr–Ti alloys in a wide

composition range [11, 28]. Large enhancement of the capacitance and permittivity of the anodic oxide films by incorporation of titanium species has been found, and the enhancement is associated with the formation of a high-temperature stable phase of cubic or tetragonal $ZrO_2$. Further increase in the titanium content results in the formation of amorphous anodic oxide films, in which film properties and film growth parameters, such as transport number of cations, change linearly with film composition.

In this work, silicon has been added to zirconium to examine the growth behavior and dielectric properties of silicon-incorporated anodic $ZrO_2$ films. Incorporation of silicon species, which are well-known glass-former, may influence the crystalline structure of the anodic oxide films, and also $ZrO_2$–$SiO_2$ is also a promising gate dielectric material for metal-oxide-semiconductor transistors [29-31].

## 2. Experimental

Zirconium and Zr–16 at.% Si alloy films, approximately 200 nm thick, were prepared by DC magnetron sputtering on to flat glass substrate as well as electropolished and subsequently anodized 99.99 % pure aluminum substrate. The target used for the preparation of the alloy films was 99.9 % zirconium disk with an appropriate number of 99.999 % silicon plates located symmetrically on the erosion region. The zirconium disk without silicon plates was used for the preparation of the zirconium films. The silicon content in the alloy was determined using TEM-EDX analysis as well as Rutherford backscattering spectroscopy (RBS).

The specimens were anodized at selected formation voltages up to 100 V for 900

s in stirred 0.1 mol $dm^{-3}$ ammonium pentaborate electrolyte at 298 K, using a two-electrode cell with a platinum counter electrode. A constant current density of 50 A $m^{-2}$ was applied before reaching the selected formation voltage. Electrochemical impedance measurements were carried out in the same electrolyte by applying 50 mV (rms) of sinusoidal alternating voltage in the $10^0$ to $10^4$ Hz range, and the capacitances of the anodic oxide films were determined by analyzing the Bode diagrams.

Vertical cross sections of the anodic oxide films were observed using a JEOL JEM-2000FX transmission electron microscope (TEM) operating at 200 kV. Electron transparent sections, about 40 nm thick, were generated using a Reichert-Nissei Ultracut S ultramicrotome with a diamond knife. The structures of the deposited zirconium and Zr–16 at.% Si alloy films as well as the anodic oxide films were identified by grazing incidence X-ray diffraction (GIXRD) using Cu Kα radiation with the incident angle of 2°. Compositions of anodic films and alloy films were determined by RBS, using a 2.0 MeV $He^{2+}$ ion beam supplied by a tandem-type accelerator at Tohoku University. The scattered particles were detected at 170° to the incident beam direction, which was normal to the specimen surface. The data were analyzed using the RUMP program. Further, depth profiling analyses of the anodic films were undertaken by glow discharge optical emission spectroscopy (GDOES) using a Jobin-Yvon 5000 RF instrument in an argon atmosphere of 850 Pa by applying RF of 13.56 MHz and power of 35 W. Light emissions of characteristic wavelengths were monitored throughout the analysis with a sampling time of 0.01 s to obtain depth profiles. The wavelengths of the spectral lines used were 339.198, 249.678, 288.158 and 130.217 nm for zirconium, boron, silicon and

oxygen respectively. The signals were detected from a circular area of approximately 4 mm diameter.

## 3. Results

### *3.1. Phases of deposited alloy films*

The GIXRD pattern of the sputter-deposited zirconium films, shown in Fig. 1, discloses an hcp structure. The Zr–16 at.% Si alloy film shows only a halo at about 35°, typical of an amorphous structure. Since no additional peaks are detected in the pattern, this alloy consists of a non-equilibrium solid solution supersaturated with silicon. Selected area electron diffraction pattern of the alloy film also showed a diffuse ring, indicating the amorphous structure. The formation of amorphous phase in the present Zr-16 at% Si alloy is in agreement with the fact that sputter-deposited binary alloys form often non-equilibrium single phase alloys in a wide composition range for a range of binary alloy systems [32].

### *3.2. Voltage-time and current-time curves*

Figure 2 shows the voltage-time curves of the zirconium and Zr–16 at.% Si alloy during initial anodizing at a constant current density of 50 A $m^{-2}$ in 0.1 mol $dm^{-3}$ ammonium pentaborate electrolyte. Both specimens show an initial voltage surge of about 2 V, reflecting the presence of thin air-formed films. After the surge, the voltages increase approximately linearly with anodizing time. The slope changes at 60 V for zirconium, probably due to increased ratio of a high-temperature form of $ZrO_2$ in the

anodic oxide films, which consist of a mixture of monoclinic and high-temperature form (cubic or tetragonal) $ZrO_2$, as discussed in the previous report [11]. The slope also changes for the Zr-16 at.% Si at 40 V from 1.9 V $s^{-1}$ to 2.3 V $s^{-1}$, probably associated with an amorphous-to-crystalline transition of the anodic oxide film, as described later.

During anodizing at constant formation voltages, current-time curves of the zirconium and Zr–16 at.% Si alloy (Fig. 3) reveal an approximately linear current decrease with time with a slope of −1 in the double logarithmic plot at both the formation voltages of 10 and 100 V, suggesting film growth at high current efficiency [33].

### *3.3. Transmission electron micrographs*

Figure 4 shows transmission electron micrographs of ultramicrotomed sections of the Zr–16 at.% Si alloy specimens anodized at several formation voltages. Obviously, the anodic oxide films, with flat and parallel alloy/film and film/electrolyte interfaces, develop on the alloy film, which appears at the bottom of micrographs. The anodic films thicken with formation voltage. The films are relatively featureless up to 30 V, indicating that the anodic oxide films are amorphous, although the anodic oxide films formed on zirconium are crystalline throughout the film thickness, as reported previously [11]. The inner ~85 % of the film thickness has slightly light appearance, due to incorporation of silicon species in this region, as revealed by later GDOES and RBS analyses. When the formation voltage increased to 40 V, an amorphous-to-crystalline transition occurs in the outer part of the anodic film and the thickness of the outer

crystalline oxide layer with respect to the total film thickness increases from 0.31 at 40 V to 0.39 at 100 V.

### *3.4. Phases in anodic oxide films*

The anodic oxide film formed on zirconium at 100 V consists of a mixture of monoclinic $ZrO_2$ and a high temperature phase of $ZrO_2$ (tetragonal or cubic), with the former being a major phase (Fig. 5). As reported previously, the relative amount of the monoclinic phase increases with an increase in the formation voltage for the anodic films formed on sputter-deposited zirconium [11]. In contrast, only the high temperature phase is detected in the GIXRD pattern of the Zr–16 at.% Si alloy anodized at 100 V. Raman spectroscopy of this specimen revealed that the crystalline phase is tetragonal [34]..

### *3.5. GDOES depth profiles*

GDOES depth profiles (Fig. 6) reveal that the anodic films formed on the Zr–16 at.% Si are not compositionally uniform in depth direction. The outer approximately 15 % of the film thickness of the anodic film formed at 20 V is apparently free from silicon species, with the relative thickness reducing to ~8 % at 100 V. In addition, for the anodic film formed at 100 V, the outer part of the silicon-containing layer appears to have lower concentration of silicon from the lower intensity of silicon in comparison with the inner part of the anodic oxide film. Boron species are incorporated into the anodic films from electrolyte, distributing mainly in the outer silicon-free layer. The

wavy profile of zirconium in the anodic film formed at 100 V is an artifact, arising from an optical interference effect caused by transparency of the film for the analyzing wavelength.

### *3.6. RBS analysis*

The compositions of the anodic films are further analyzed quantitatively using RBS analysis. Figure 7 shows the experimental and simulated spectra for the Zr–16 at.% Si anodized at 30, 50 and 100 V. The simulated spectrum obtained using the thickness and composition for each layer, shown in Table 1, fitted well with the experimental spectrum. In this simulation, boron species incorporated into the anodic film are neglected due to its low sensitivity and low concentration. Figure 7(d) shows the enlarged yield from silicon for the specimen anodized at 100 V, revealing clearly the presence of two silicon-containing layers with different silicon concentrations. Simulation for the specimen anodized to 100 V reveals that the outermost layer of 15 nm thickness is free from silicon species and the composition of the intermediate layer of 48 nm thickness is $(Zr_{0.88}Si_{0.12})O_2$. From the comparison with the TEM image in Fig. 4, these two layers are crystalline. The remaining inner layer, which is amorphous, has a composition of $(Zr_{0.82}Si_{0.18})O_2$. The density of the outer $ZrO_2$ layer is 5.8 Mg $m^{-3}$, being in agreement with that of bulk crystalline $ZrO_2$ [35]. The inner layer has lower density, due to increased silicon concentration as well as amorphous structure. From the comparison of the charges in the films, obtained from RBS analysis, with that passed in anodizing the specimen at each formation voltage, the current efficiency for film growth

is close to 100 %. Further, the ratio of the number of $Si^{4+}$ ions to the sum of the numbers of $Zr^{4+}$ and $Si^{4+}$ ions in the anodic film formed at 100 V is 0.15, in agreement with the alloy composition.

At the formation voltage of 50 V, similar three-layer film is developed (Table 1). The thickness of the outer silicon-free layer at 50 V is similar to that formed at 100 V, although the inner silicon-containing layer is thicker at the latter formation voltage. Only two-layer is resolved for the anodic oxide film formed at 30 V. No intermediate layer with the lower silicon content is present at this formation voltage, probably due to the absence of crystalline oxide layer.

### *3.7. Impedance measurements and dielectric properties*

Capacitances of the anodic oxide films formed on the zirconium and Zr–16 at.% Si alloy to various formation voltages are determined from electrochemical impedance measurements. Figure 8 shows the Bode diagrams of the sputter-deposited Zr–16 at.% Si alloy anodized to various formation voltages. All specimens show the similar behavior of linear change in impedance with a slope close to −1 and phase shift to −90 ° in the wide frequency region. The behavior is typical of dielectric materials. The impedance data were curve fitted using the equivalent electric circuit inserted in Fig. 8.

Figure 9 shows the relationship between the reciprocal capacitance of anodic oxide films and the film formation voltage for zirconium and Zr–16 at.% Si alloy. The reciprocal capacitance of anodic oxide films on zirconium increases linearly with formation voltage, since the capacitance is inversely proportional to the film thickness.

However, in the case of the anodic oxide films formed on Zr–16 at.% Si alloy, the slope changes at 30-40 V, with the slope decreasing at higher formation voltages, probably associated with the change in film structure. The enhanced capacitance of the anodic zirconium oxide film by addition of silicon is evident from this figure, particularly at higher film formation voltages. The capacitance of the anodic oxide film formed on Zr–16 at.% Si alloy is 1.44 times that on zirconium at 100 V.

## 4. Discussion

### *4.1.* An amorphous-to-crystalline transition of anodic oxide films

In contrast to the formation of crystalline anodic oxide films on zirconium [11], the anodic films formed on the present Zr–16 at.% Si single phase alloy is amorphous at low formation voltages up to 30 V. Silicon species are well-known glass-former, such that the incorporation of silicon species in the anodic oxide films from substrate stabilizes amorphous structure. However, the silicon species are not distributed uniformly throughout the film thickness, incorporating only in the inner approximately 85 % of the film thickness. The outer ~15 % of the film thickness is free from silicon species, but the film are amorphous throughout the film thickness up to 30 V.

At the formation voltages above 30 V, an amorphous-to-crystalline transition occurs in the outer part of the anodic oxide films with the thickness of the crystalline layer, relative to the total film thickness, increasing with the formation voltage (Fig. 10). The transition may be initiated in the film region free from silicon species, extending to the outer part of the silicon-containing layer. In general, anodic oxide films thicken

linearly with formation voltage, but the thickness of the anodic film formed on the present alloy at 100 V deviates obviously from the linear correlation, observed at lower formation voltages. The deviation to the thinner side suggests that the crystalline oxide layer sustains the higher electric field compared with the amorphous layer.

An amorphous-to-crystalline transition has been found during anodizing of titanium and its alloys [20, 36], niobium [37, 38] and tantalum [39, 40]. The importance of an air-formed oxide, which is present before anodizing, in the amorphous-to-crystalline transition of anodic niobium oxide [41] and silicon-incorporated anodic titanium oxide [20, 42] has been reported; due to the presence of precursor of crystalline nuclei in the air-formed oxide, crystalline oxide is developed at the site where the air-formed oxide is located during film growth at a high electric field. In the present anodic oxide films formed on the Zr-16 at.% Si, the amorphous-to-crystalline transition may occur, similar to the anodic oxide films on niobium and Ti-Si alloy.

### *4.2. Structure of anodic oxide films*

The amorphous-to-crystalline transition of the anodic oxide films on the Zr–16 at.% Si alloy develops tetragonal phase of $ZrO_2$, in contrast to the formation of mainly monoclinic $ZrO_2$ on zirconium. The tetragonal phase is a high-temperature stable phase, and it is well known that this phase can be stabilized to ambient temperature by incorporation of foreign species with lower valents, such as $Mg^{2+}$, $Ca^{2+}$ and $Y^{3+}$ or by reducing the grain size to less than 30 nm [43]. From TEM images shown in Fig. 4, the

grain size of the crystalline anodic oxide layers formed on the present alloy is apparently less than 30 nm. Such small grain size may be at least one of the reasons for the formation of the high-temperature stable phase.

The anodic oxide films formed on the Zr–16 at.% Si up to 30 V and the inner part of the anodic oxide films above 30 V are amorphous. When magnetron-sputtered zirconium is anodized, crystalline anodic oxide films are developed even at low formation voltages. Foreign species can be incorporated into anodic zirconium oxide from substrate, inducing the formation of amorphous oxide. The anodic oxide films formed on a Zr–20 at.% Ti alloy is crystalline throughout the film thickness [11], while the anodic oxide films formed on the present Zr–16 at.% Si are amorphous throughout the film thickness up to 30 V and within the inner 60 % or more of the film thickness at and above 40 V. Thus, amorphous phase is more readily formed in the anodic zirconium oxide by incorporation of silicon species rather than that of titanium species. This result should be related to the mobility of silicon and titanium species, i.e., the former immobile and the latter mobile outwards, in growing anodic oxide films, as in anodic titanium oxide.

Crystallization of anodic titanium oxide can also be suppressed by incorporation of foreign species, such as aluminum , molybdenum [44], silicon [45, 46], tungsten [47] and zirconium [28] from substrate. Silicon species are the most effective in suppressing the crystallization; the addition of only 6 at.% silicon to titanium is enough to grow an amorphous anodic oxide to more than 100 V. In contrast, on Ti–Al alloys, an amorphous oxide grows to more than 100 V only when more than 20 at.% aluminum is added to

titanium. Such trend is in agreement with the mobility of foreign species; slower migrating or immobile species, like silicon species, which has a strong metal-oxygen bond, suppress more effectively the crystallization of anodic titania [48].

### *4.3. Ionic transport in growing anodic oxide films*

It is known that silicon species are immobile in a range of growing anodic oxides, including aluminum oxide [49], niobium oxide [50], tantalum oxide [51, 52], titanium oxide [45, 46]. Thus, it is likely that silicon species are immobile also in growing anodic zirconium oxide, acting as marker species. In this case, a silicon-free outer layer of anodic oxide films on a Zr–Si alloy is developed at the film/electrolyte interface by migration of zirconium ions outwards, while the remaining silicon-containing inner layer is formed at the alloy/film interface by migration of $O^{2-}$ ions inwards. The transport number of cations, $t^+$, can be estimated from the RBS results using a following equation;

$$t^+ = N_{out} / N_t$$

where $N_{out}$ is the number of cations in the outer silicon-free layer, and $N_t$ is the number of cations in the anodic oxide film. The transport number of cations obtained from the RBS data for the anodic oxide film formed at 30 V, which is amorphous, is 0.16, which is in agreement with that estimated for the amorphous zirconium oxide from the extrapolation of the compositional dependence of the transport number of cations for the amorphous anodic oxide films formed on a range of Ti–Zr alloys [28]. This suggests that the incorporation of silicon species in amorphous oxide does not influence the

transport number, although for amorphous anodic oxides composed of two cations, both of which migrate outwards in film growth, the transport number of cations generally changes with film composition. In contrast, the transport number of cations, obtained from the anodic film formed at 100 V, is reduced to be 0.09, due to the formation of crystalline oxide, in which anion migration is generally predominant.

A characteristic feature of the anodic oxide films after crystallization is the presence of an intermediate layer with lower silicon content in comparison with that in the innermost layer. The formation of the intermediate layer should be associated with the different transport number of cations in the outer crystalline layer and in the inner amorphous layer. During growth of amorphous anodic oxide below 40 V, new film materials are formed both at the film/electrolyte and alloy/film interface by migration of $Zr^{4+}$ ions outwards and $O^{2-}$ ions inwards, respectively (Fig. 11(a)). After crystallization of the outer part of the anodic films, the inward migration of $O^{2-}$ ions must become predominant in the outer crystalline layer, while both $Zr^{4+}$ ions and $O^{2-}$ ions migrate outwards and inward, respectively, in the inner amorphous layer. Since the cation migration in the outer crystalline layer is very limited, $Zr^{4+}$ ions that reach at the boundary between the outer crystalline layer and an inner amorphous layer, may form new $ZrO_2$ with $O^{2-}$ ions migrating from the outer layer to the boundary (Fig. 11(b,c)). Due to the formation of new $ZrO_2$ at the boundary, the concentration of silicon species decreases, such that the intermediate oxide layer with lower silicon content is developed. Once the intermediate layer is developed, the thickness of the outer crystalline $ZrO_2$ layer free from silicon species is unchanged, and the thicknesses of the intermediate

crystalline layer and innermost amorphous layer increase due to development of new film materials at the boundary between the amorphous and crystalline layers and at the alloy/film interface, respectively.

### *4.4. Dielectric properties*

As shown in Fig. 9, the capacitances of anodic oxide films are enhanced by the addition of silicon, particularly at the formation voltages higher than 30 V. However, the addition of silicon does not increase the relative permittivity of the anodic oxide films (Fig. 12). The relative permittivity of the anodic oxide films, $\varepsilon_{ox}$, was derived using the following equation:

$$C = \varepsilon_0 \, \varepsilon_{ox} / d$$

in which, $\varepsilon_0$ is permittivity of vacuum and $d$ is the thickness of anodic oxide film. The capacitance per unit surface are, C, was obtained by AC impedance analysis and the thickness of the anodic oxide films on the Zr-16 at% Si was obtained by cross-sectional TEM observation. Since the film growth proceeds at high current efficiency, the thickness of anodic oxide films on zirconium was calculated from the charge passed during anodizing using the density of anodic zirconium oxide of 5.8 Mg $m^{-3}$ [21]. The relative permittivity of anodic oxide films on zirconium is around $\varepsilon_{ox}$ = 22.7, and this is comparable to values reported previously ($\varepsilon_{ox}$ = 22-25). The average relative permittivity of the anodic oxide films on Zr–16 at.% Si alloy is 21.7, being slightly smaller than that of zirconium. The reduction in permittivity may be due to the lower relative permittivity of $SiO_2$ ($\varepsilon_{ox}$ = 3.5) incorporated into anodic oxide. The reduction of

the relative permittivity by incorporation of silicon species is also reported for amorphous $TiO_2$ [42] and $Nb_2O_5$ [50].

The increased capacitance of the anodic oxide films by the addition of silicon is, therefore, due to the reduction of film thickness. In Fig. 10, the slope of the film thickness vs formation voltage curve corresponds to the formation ratio. The formation ratio changes from 1.87 nm $V^{-1}$ below 40 V to 1.34 nm $V^{-1}$ at and above 40 V for the Zr-16 at% Si. The formation ratio for the anodic oxide films on zirconium was constant up to 100 V, being 2.5 nm $V^{-1}$. The markedly reduced formation ratio by the addition of silicon, particularly at and above 40 V, at which a crystalline oxide layer is developed, enhances the capacitance the capacitance.

## 5. Conclusions

Through the examination of growth and electric properties of anodic oxide films formed on the Zr–16 at.% Si single phase solid solution alloy in ammonium pentaborate electrolyte at high current efficiency, following conclusions are drawn.

1. The anodic oxide films formed on the Zr–16 at.% Si are amorphous up to 30 V, in contrast to the formation of crystalline oxide films on zirconium. At higher formation voltages, the outer part of the anodic oxide films crystallizes with the relative thickness of the crystalline layer increasing to ~40 % at 100 V. The outer crystalline layer consists of a high-temperature stable tetragonal phase of $ZrO_2$.
2. The outer layer, 16 % or less of the film thickness, is composed of silicon-free oxide. This layer is formed due to immobile nature of silicon species in growing

amorphous anodic oxide, in which film growth proceeds due to simultaneous migrations of $Zr^{4+}$ ions outwards and $O^{2-}$ ions inwards.

3. In addition to crystalline outer layer free from silicon species, an intermediate crystalline oxide layer, in which silicon content is lower than that in the inner amorphous layer, is developed, due to $ZrO_2$ formation at the boundary of the crystalline layer and amorphous layer.
4. Capacitance of the anodic oxide films are highly enhanced by incorporation of silicon species due to reduced film thickness at selected formation voltages, even though the permittivity of anodic oxide decreases with silicon incorporation. The capacitance is further enhanced by crystallization of anodic oxide.

**Acknowledgement**

The present work was supported in part by the Global COE Program (Project No. B01: Catalysis as the Basis for Innovation in Materials Science) from the Ministry of Education, Culture, Sports, Science and Technology, Japan.

**References**

[1] R.H.J. Hannink, P.M. Kelly, B.C. Muddle, J. Am. Ceram. Soc., 83 (2000) 461.

[2] S.P.S. Badwal, Solid State Ionics, 52 (1992) 23.

[3] K.E. Sickafus, H. Matzke, T. Hartmann, K. Yasuda, J.A. Valdez, P. Chodak, M. Nastasi, R.A. Verrall, J. Nucl. Mater., 274 (1999) 66.

[4] C.M. Perkins, B.B. Triplett, P.C. McIntyre, K.C. Saraswat, S. Haukka, M.

Tuominen, Appl. Phys. Lett., 78 (2001) 2357.

[5] V. Fiorentini, G. Gulleri, Phys. Rev. Lett., 89 (2002)

[6] W.J. Qi, R. Nieh, B.H. Lee, L.G. Kang, Y. Jeon, J.C. Lee, Appl. Phys. Lett., 77 (2000) 3269.

[7] J.P. Chang, Y.S. Lin, K. Chu, J. Vac. Sci. Technol. B, 19 (2001) 1782.

[8] A. Hardy, S. Van Elshocht, C. Adelmann, T. Conard, A. Franquet, O. Douheret, I. Haeldermans, J. D'Haen, S. De Gendt, M. Caymax, M. Heyns, M. D'Olieslaeger, M.K. Van Bael, J. Mullens, Thin Solid Films, 516 (2008) 8343.

[9] S. Van Elshocht, A. Hardy, C. Adelmann, M. Caymax, T. Conard, A. Franquet, O. Richard, M.K. Van Bael, J. Mullens, S. De Gendt, J. Electrochem. Soc., 155 (2008) G91.

[10] M. Kamijyo, T. Onozuka, S. Shinkai, K. Sasaki, M. Yamane, Y. Abe, Jpn. J. Appl. Phys., 42 (2003) 4399.

[11] H. Habazaki, K. Shimizu, S. Nagata, K. Asami, K. Takayama, Y. Oda, P. Skeldon, G.E. Thompson, Thin Solid Films, 479 (2005) 144.

[12] V. Zwilling, E. Darque-Ceretti, A. Boutry-Forveille, D. David, M.Y. Perrin, M. Aucouturier, Surf. Interface Anal., 27 (1999) 629.

[13] D. Gong, C.A. Grimes, O.K. Varghese, W.C. Hu, R.S. Singh, Z. Chen, E.C. Dickey, J. Mater. Res., 16 (2001) 3331.

[14] H. Tsuchiya, J.M. Macak, I. Sieber, L. Taveira, A. Ghicov, K. Sirotna, P. Schmuki, Electrochem. Commun., 7 (2005) 295.

[15] H. Tsuchiya, P. Schmuki, Electrochem. Commun., 6 (2004) 1131.

[16] W. Wei, J.M. Macak, P. Schmuki, Electrochem. Commun., 10 (2008) 428.

[17] A. Ghicov, P. Schmuki, Chem. Commun., (2009) 2791.

[18] I. Sieber, H. Hildebrand, A. Friedrich, P. Schmuki, Electrochem. Commun., 7 (2005) 97.

[19] C.K. Dyer, J.S.L. Leach, J. Electrochem. Soc., 125 (1978) 1032.

[20] H. Habazaki, M. Uozumi, H. Konno, K. Shimizu, P. Skeldon, G.E. Thompson, Corros. Sci., 45 (2003) 2063.

[21] J.P.S. Pringle, Electroche. Acta, 25 (1980) 1420.

[22] L. Young, D.J. Smith, J. Electrochem.Soc., 126 (1979) 765.

[23] J.A. Davies, B. Domeij, J.P.S. Pringle, F. Brown, J. Electrochem. Soc., 112 (1965) 675.

[24] N. Khalil, J.S.L. Leach, J. Appl. Electrochem., 26 (1996) 231.

[25] Y. Kurima, G.E. Thompson, K. Shimizu, G.C. Wood, Proc. Int. Symp. Oxide Films on Metals and Alloys, K.R. Hebert, G.E. Thompson (eds.), The Electrochemical Society, Pennington, p.256, 1994.

[26] P.H.G. Draper, J. Harvey, Acta Met., 11 (1963) 873.

[27] C. Panagopoulos, Mater. Lett., 3 (1985) 393.

[28] H. Habazaki, M. Uozumi, H. Konno, K. Shimizu, S. Nagata, K. Asami, K. Matsumoto, K. Takayama, Y. Oda, P. Skeldon, G.E. Thompson, Electrochim. Acta, 48 (2003) 3257.

[29] D.A. Neumayer, E. Cartier, J. Appl. Phys., 90 (2001) 1801.

[30] H. Kim, P.C. McIntyre, J. Appl. Phys., 92 (2002) 5094.

[31] S. Stemmer, Z.Q. Chen, C.G. Levi, P.S. Lysaght, B. Foran, J.A. Gisby, J.R. Taylor, Jpn. J. Appl. Phys., 42 (2003) 3593.

[32] K. Hashimoto, P.Y. Park, J.H. Kim, H. Yoshioka, H. Mitsui, E. Akiyama, H. Habazaki, A. Kawashima, K. Asami, Z. Grzesik, S. Mrowec, Mater. Sci. Eng. A, 198 (1995) 1.

[33] P. Meisterjahn, U. Konig, J.W. Schultze, Electrochim. Acta, 34 (1989) 551.

[34] S. Koyama, Y. Aoki, H. Habazaki, to be submitted,

[35] D.R. Lide, ed. *CRC Handbook of Chemistry and Physics, 73rd Edition* 1992, CRC Press, p..4-113.

[36] T. Shibata, Y.-C. Zhu, Corros. Sci., 37 (1995) 253.

[37] D.M. Lakhiani, L.L. Shreir, Nature, 188 (1960) 49.

[38] N.F. Jackson, J.C. Hendy, Electrocomponent Sci. Technol., 1 (1974) 27.

[39] D.A. Vermilyea, J. Electrochem. Soc., 102 (1955) 207.

[40] N.F. Jackson, J. Appl. Electrochem., 3 (1973) 91.

[41] H. Habazaki, T. Ogasawara, H. Konno, K. Shimizu, S. Nagata, P. Skeldon, G.E. Thompson, Corros. Sci., 49 (2007) 580.

[42] M.T. Tanvir, K. Fushimi, K. Shimizu, S. Nagata, P. Skeldon, G.E. Thompson, H. Habazaki, Electrochim. Acta, 52 (2007) 6834.

[43] R.C. Garvie, J. Phys. Chem., 69 (1965) 1238.

[44] H. Habazaki, M. Uozumi, H. Konno, K. Shimizu, S. Nagata, K. Asami, P. Skeldon, G.E. Thompson, Electrochim. Acta, 47 (2002) 3837.

[45] H. Habazaki, K. Shimizu, S. Nagata, P. Skeldon, G.E. Thompson, G.C. Wood,

Corros. Sci., 44 (2002) 1047.

[46] H. Habazaki, K. Shimizu, S. Nagata, P. Skeldon, G.E. Thompson, G.C. Wood, J. Electrochem. Soc., 149 (2002) B70.

[47] H. Habazaki, M. Uozumi, H. Konno, K. Shimizu, S. Nagata, K. Takayama, Y. Oda, P. Skeldon, G.E. Thompson, J. Electrochem. Soc., 152 (2005) B263.

[48] H. Habazaki, H. Konno, K. Shimizu, J. Surf. Finish. Soc. Jpn., 54 (2003) 456.

[49] G.C. Wood, P. Skeldon, G.E. Thompson, K. Shimizu, J. Electrochem.Soc., 143 (1996) 74.

[50] H. Habazaki, T. Matsuo, H. Konno, K. Shimizu, S. Nagata, K. Matsumoto, K. Takayama, Y. Oda, P. Skeldon, G.E. Thompson, Electrochim. Acta, 48 (2003) 3519.

[51] K. Shimizu, K. Kobayashi, P. Skeldon, G.E. Thompson, G.C. Wood, Phil. Mag. A, 72 (1995) 1409.

[52] K. Shimizu, K. Kobayashi, G.E. Thompson, P. Skeldon, G.C. Wood, Philos. Mag. B, 73 (1996) 461.

**Figure captions**

Fig. 1 Grazing incidence X-ray diffraction patterns of the sputter-deposited zirconium and Zr–16 at.% Si alloy.

Fig. 2 Voltage-time responses of the sputter-deposited zirconium and Zr–16 at.% Si alloy during initial anodizing at a constant current density of 50 A $m^{-2}$ in 0.1 mol $dm^{-3}$ ammonium pentaborate electrolyte at 298 K.

Fig. 3 Current-time curves of the sputter-deposited zirconium and Zr–16 at.% Si alloy during anodizing at 10 V and 100 V in 0.1 mol $dm^{-3}$ ammonium pentaborate electrolyte at 298 K. Initially, a constant current density of 50 A $m^{-2}$ was applied to reach the selected formation voltage. In this plot, the anodizing time of 0 s was set at the time when the formation voltage reached the selected formation voltage.

Fig. 4 Transmission electron micrographs of ultramicrotomed sections of the sputter-deposited Zr–16 at.% Si alloy, after anodizing at (a) 10 V, (b) 20 V, (c) 30 V, (d) 40 V, (e) 50 V, and (f) 100 V in 0.1 mol $dm^{-3}$ ammonium pentaborate electrolyte at 298 K for 900 s, following constant current anodizing at 50 A $m^{-2}$ to respective formation voltages.

Fig. 5 Grazing incidence X-ray diffraction patterns of the sputter-deposited zirconium and Zr–16 at.% Si alloy specimens anodized at 100 V in 0.1 mol $dm^{-3}$ ammonium

pentaborate electrolyte at 298 K for 900 s, following constant current anodizing at 50 A $m^{-2}$ to the selected formation voltage.

Fig. 6 GDOES depth profiles of the anodic films formed on sputter-deposited Zr–16 at.% Si alloy at (a) 20 V, and (b) 100 V in 0.1 mol $dm^{-3}$ ammonium pentaborate electrolyte at 298 K for 900 s, following constant current anodizing at 50 A $m^{-2}$ to the respective formation voltages.

Fig. 7 Experimental and simulated RBS spectra of the sputter-deposited Zr–16 at.% Si alloy anodized at (a) 30 V, (b) 50 V and (c, d) 100 V in 0.1 mol $dm^{-3}$ ammonium pentaborate electrolyte at 298 K for 900 s, following constant current anodizing at 50 A $m^{-2}$ to the respective formation voltages.

Fig. 8 Bode diagrams of the sputter-deposited Zr–16 at.% Si alloy specimens anodized at 10, 20, 50, and 100 V in 0.1 mol $dm^{-3}$ ammonium pentaborate electrolyte at 298 K for 900 s, following constant current anodizing at 50 A $m^{-2}$ to the respective formation voltage.

Fig. 9 The formation voltage dependence of the reciprocal of capacitance of the anodic oxide films, formed on the sputter-deposited zirconium and Zr–16 at.% Si alloy in 0.1 mol $dm^{-3}$ ammonium pentaborate electrolyte at 298 K.

Fig. 10 Film thickness, obtained by the cross-sectional TEM observations, of the anodic oxide films formed on Zr–16 at.% Si alloy in 0.1 mol $dm^{-3}$ ammonium pentaborate electrolyte at 298 K, versus formation voltage.

Fig. 11 Schematic illustration showing the growth of anodic oxide films on the Zr-16 at.% Si alloy. (a) amorphous oxide before crystallization, (b) after amorphous-to-crystalline transition, (c) film formation at the boundary between outer crystalline and inner amorphous layers.

Fig. 12 Relative permittivity of the anodic oxide films formed on zirconium and Zr–16 at.% Si alloy in 0.1 mol $dm^{-3}$ ammonium pentaborate electrolyte at 298 K, versus formation voltage.

Fig. 1

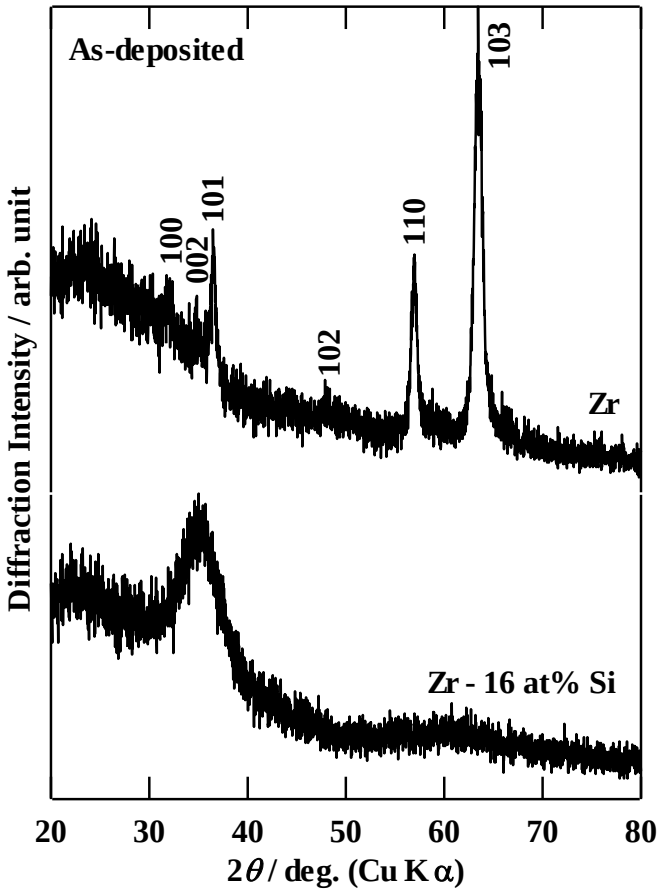
As-deposited
100
002
101
102
110
103
Zr
Zr - 16 at% Si
Diffraction Intensity / arb. unit
20
30
40
50
60
70
80
2θ / deg. (Cu Kα)

Fig. 2

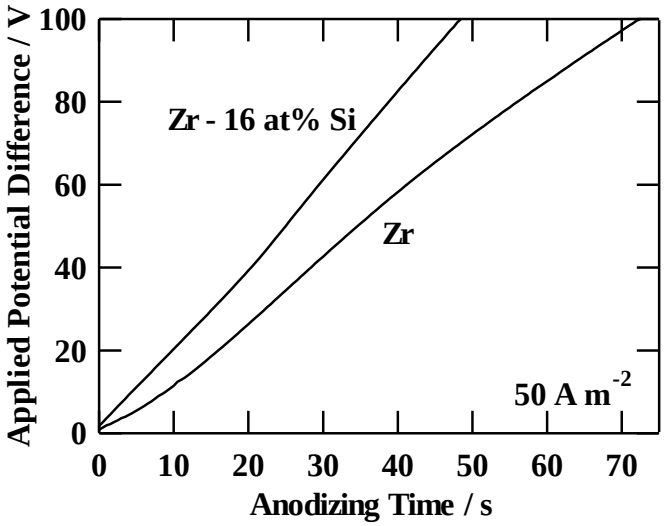
Applied Potential Difference / V
100
80
60
40
20
0
0
10
20
30
40
50
60
70
Anodizing Time / s
Zr - 16 at% Si
Zr
50 A m-2

Fig. 3

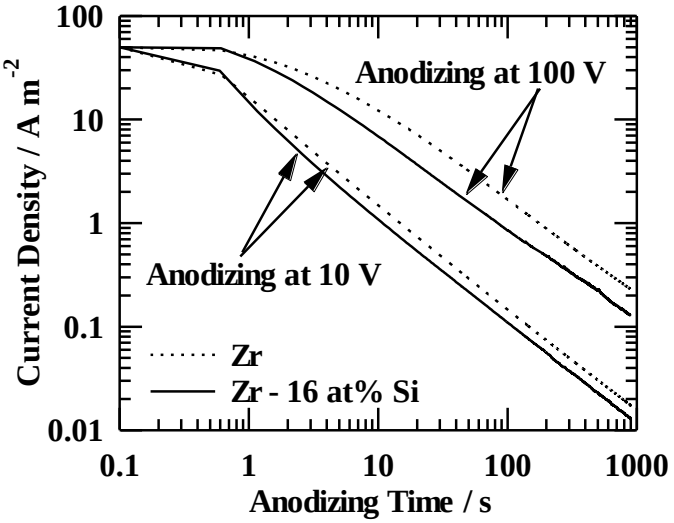
100
10
1
0.1
0.01
0.1
1
10
100
1000
Current Density / A m-2
Anodizing Time / s
Anodizing at 100 V
Anodizing at 10 V
Zr
Zr - 16 at% Si

Fig. 4

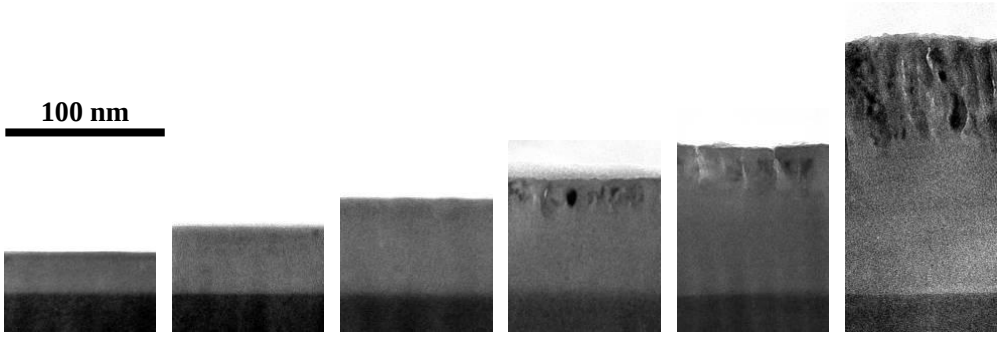


**(a) 10 V** **(b) 20 V** **(c) 30 V** **(d) 40 V** **(e) 50 V** **(f) 100 V**

Fig. 5

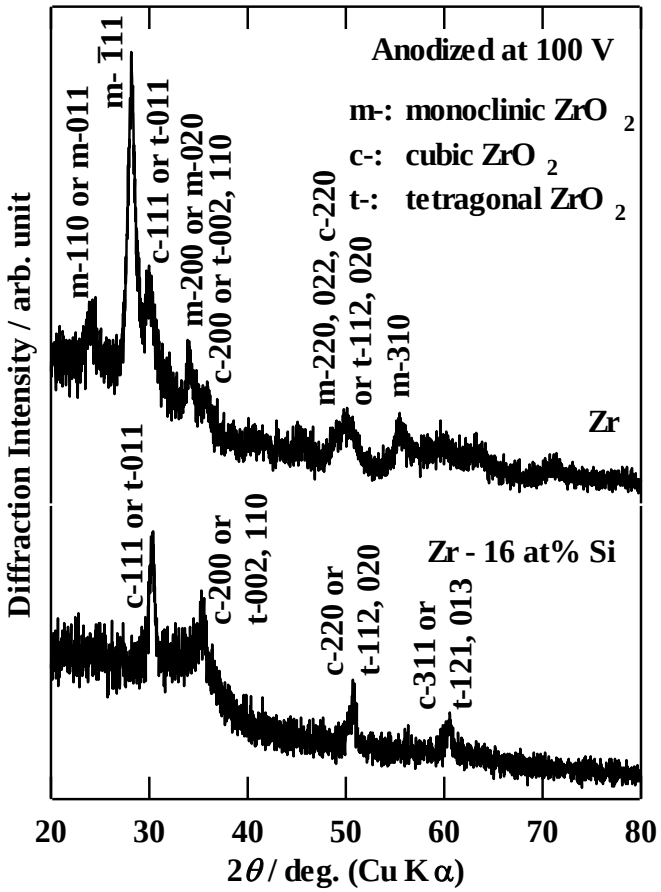
Anodized at 100 V
m-: monoclinic ZrO 2
c-: cubic ZrO 2
t-: tetragonal ZrO 2
m-110 or m-011
m- $\bar{1}$11
c-111 or t-011
m-200 or m-020
c-200 or t-002, 110
m-220, 022, c-220
or t-112, 020
m-310
Zr
c-111 or t-011
c-200 or
t-002, 110
c-220 or
t-112, 020
c-311 or
t-121, 013
Zr - 16 at% Si
Diffraction Intensity / arb. unit
20
30
40
50
60
70
80
2θ / deg. (Cu Kα)

Fig. 6

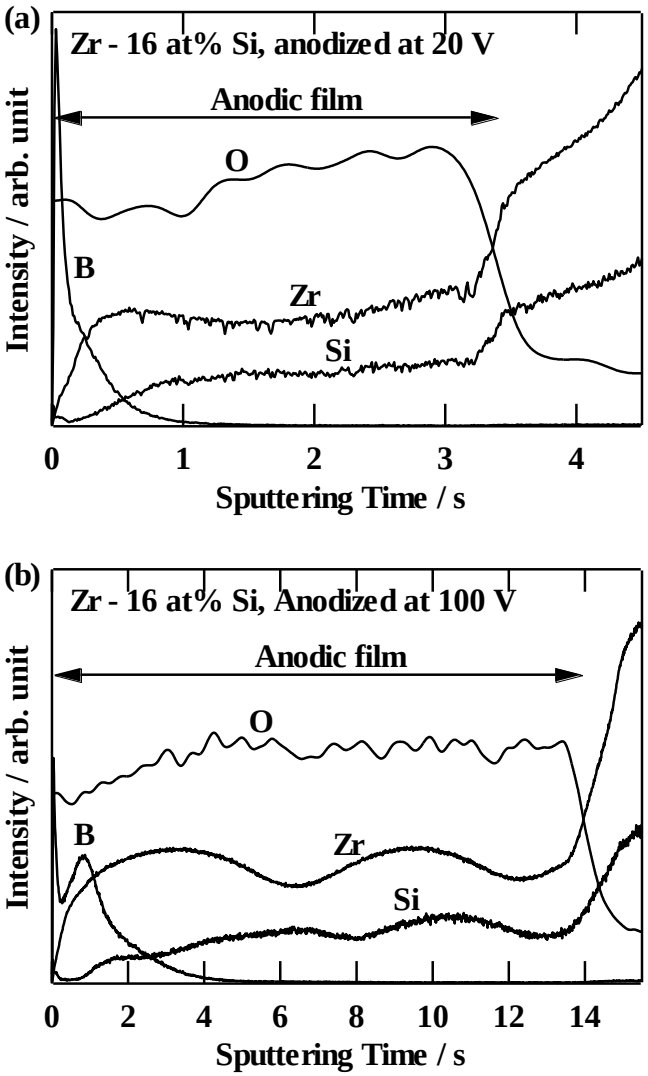
(a)
Zr - 16 at% Si, anodized at 20 V
Anodic film
O
B
Zr
Si
Intensity / arb. unit
0
1
2
3
4
Sputtering Time / s
(b)
Zr - 16 at% Si, Anodized at 100 V
Anodic film
O
B
Zr
Si
Intensity / arb. unit
0
2
4
6
8
10
12
14
Sputtering Time / s

Fig. 7

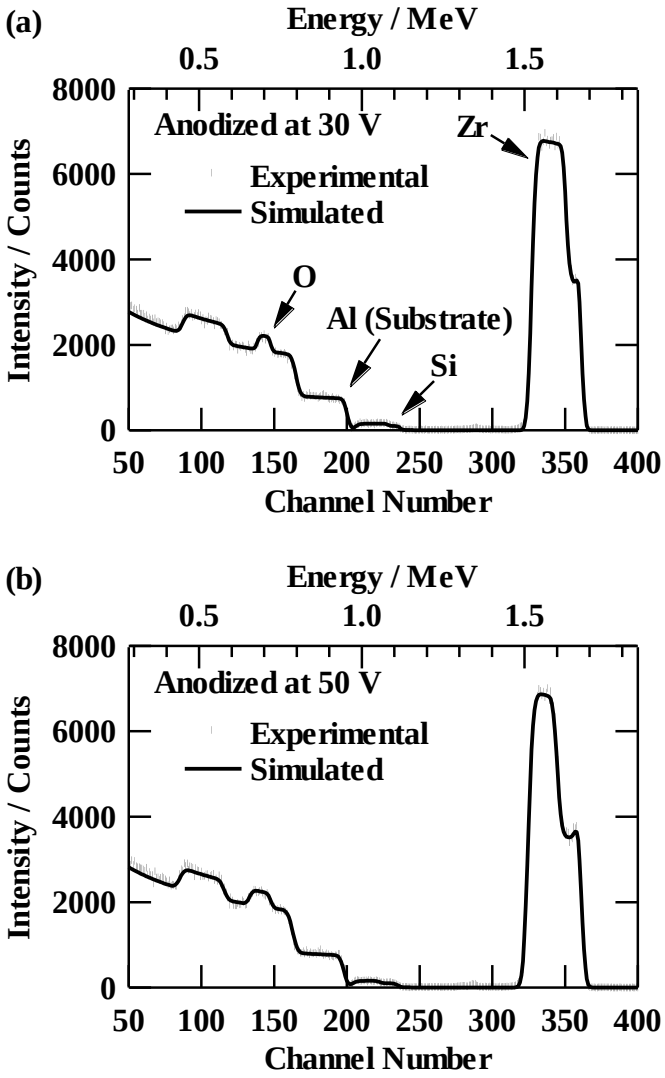
(a)
Energy / MeV
0.5
1.0
1.5
8000
6000
4000
2000
0
Anodized at 30 V
Experimental
Simulated
Zr
O
Al (Substrate)
Si
Intensity / Counts
50
100
150
200
250
300
350
400
Channel Number
(b)
Energy / MeV
0.5
1.0
1.5
8000
6000
4000
2000
0
Anodized at 50 V
Experimental
Simulated
Intensity / Counts
50
100
150
200
250
300
350
400
Channel Number

Fig. 7 (Continued)

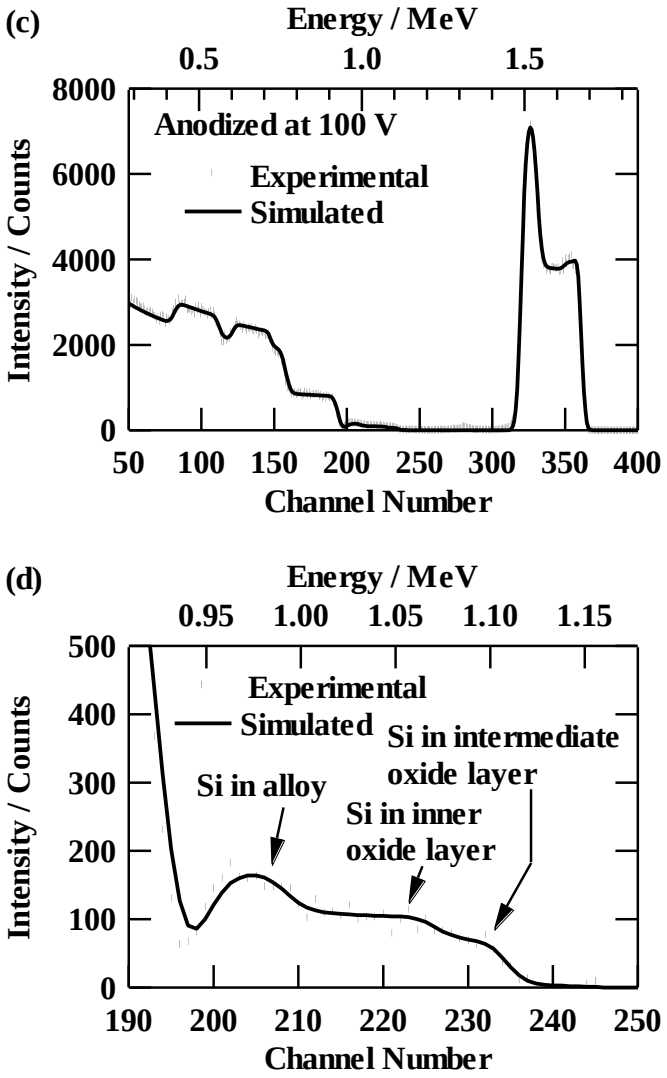

Fig. 8

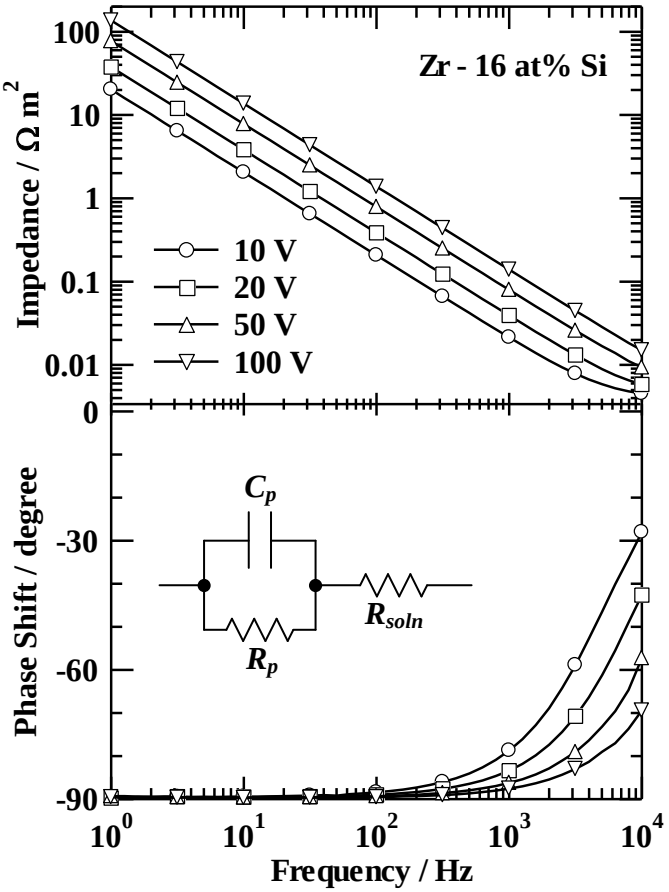
Zr - 16 at% Si
Impedance / Ω m 2
100
10
1
0.1
0.01
0
10 V
20 V
50 V
100 V
Phase Shift / degree
-30
-60
-90
$C_p$
$R_{soln}$
$R_p$
$10^0$
$10^1$
$10^2$
$10^3$
$10^4$
Frequency / Hz

Fig. 9

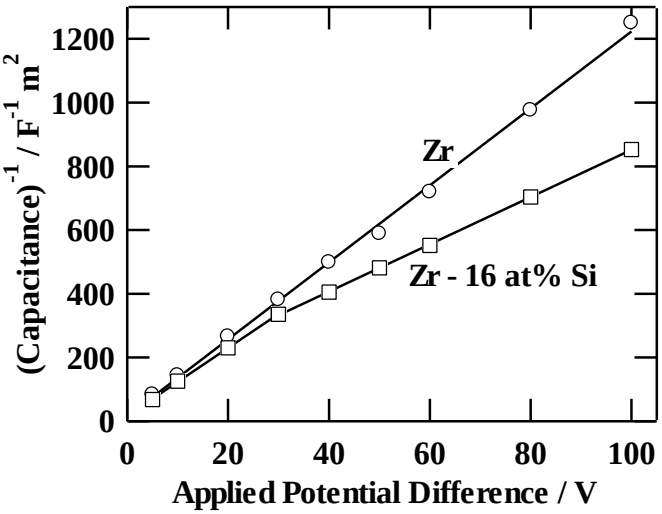
(Capacitance)$^{-1}$ / F$^{-1}$ m$^2$
1200
1000
800
600
400
200
0
0
20
40
60
80
100
Applied Potential Difference / V
Zr
Zr - 16 at% Si

Fig. 10

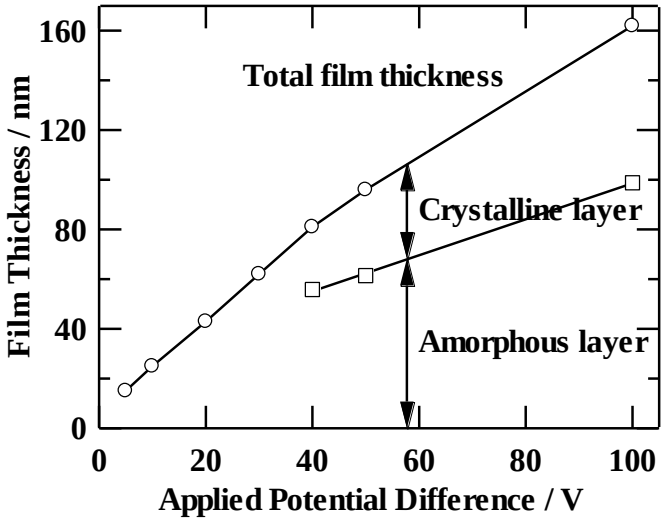
Film Thickness / nm
160
120
80
40
0
0
20
40
60
80
100
Applied Potential Difference / V
Total film thickness
Crystalline layer
Amorphous layer

Fig. 11

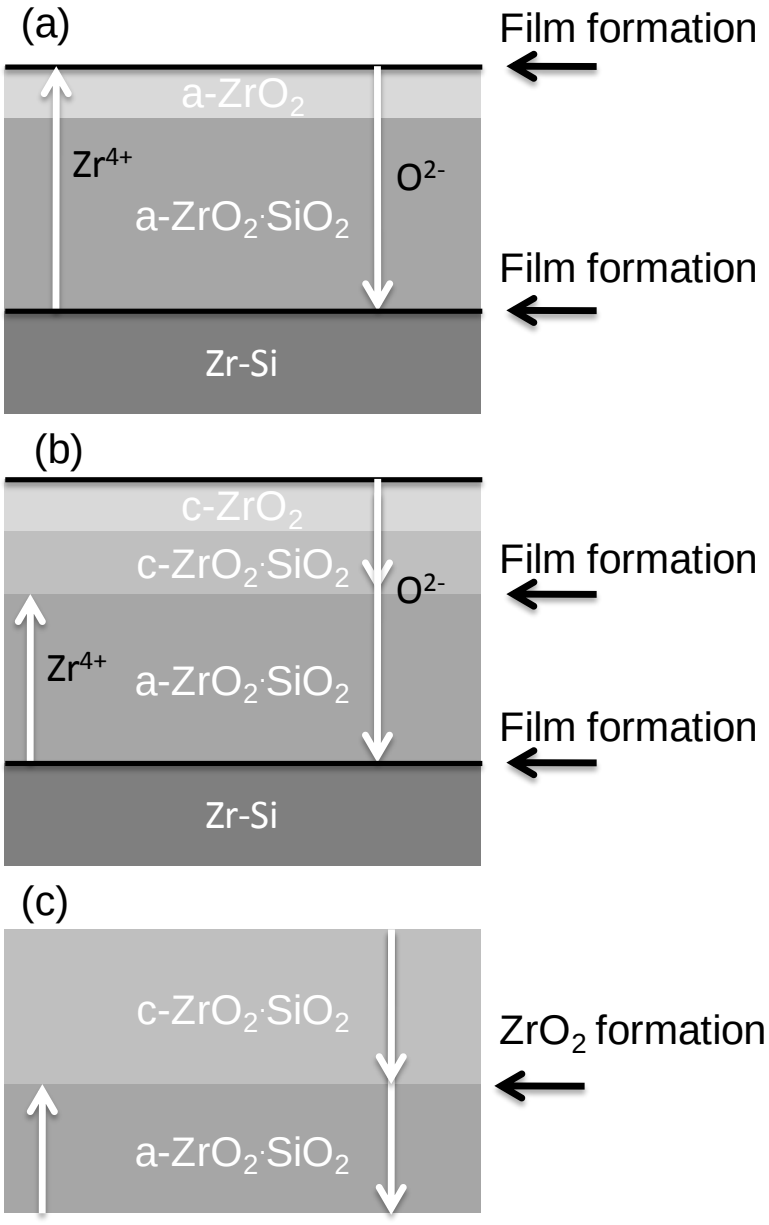
(a)
Film formation
a-ZrO2
Zr4+
O2-
a-ZrO2·SiO2
Film formation
Zr-Si
(b)
c-ZrO2
c-ZrO2·SiO2
Film formation
O2-
Zr4+
a-ZrO2·SiO2
Film formation
Zr-Si
(c)
c-ZrO2·SiO2
ZrO2 formation
a-ZrO2·SiO2

Fig. 12

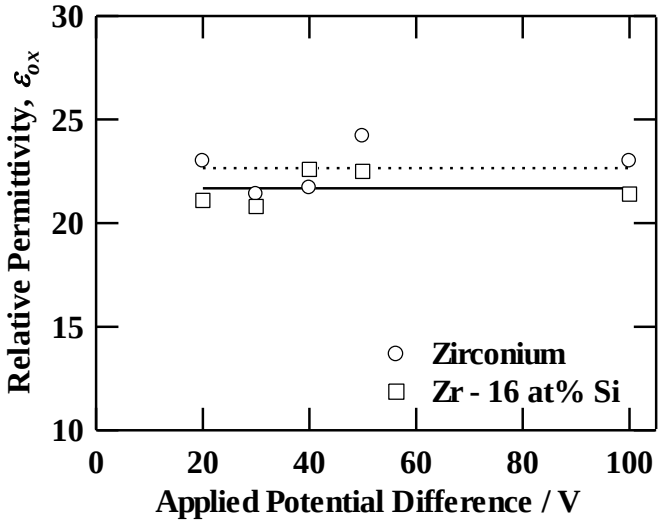
Relative Permittivity, $\varepsilon_{ox}$
30
25
20
15
10
0
20
40
60
80
100
Applied Potential Difference / V
Zirconium
Zr - 16 at% Si